

The use of multiscale materials modelling within the UK nuclear industry

P.E.J. Flewitt*

Reactor Services Organisation, BNFL Magnox Generation, Berkeley Glos, Gloucestershire GL13 9PB, UK

Abstract

The continued safe operation of high integrity structures and components in the nuclear industry is assured by using arguments which are usually based upon deterministic methodologies. These require theoretical models to provide the input parameters or the necessary mechanistic understanding of the mechanical or physical properties. Consideration is given to modelling that has been used for one class of reactor type power stations, Magnox. Modelling to provide key parameters for input to the safety cases are discussed. The models adopted span many orders of magnitude from the atomic scale to those providing a description of aspects of complete engineering structures. At the atomic scale these provide an insight to the production of point defect damage in steels as a result of exposure to a neutron spectrum containing fast and thermalised neutrons and the subsequent effects of both temperature and neutron dose. In addition equilibrium and non-equilibrium segregation of alloying and impurity atom species to grain boundaries is modelled. Both are necessary for understanding the changes in fracture and mechanical properties for these steels after extended periods of service. At the microstructural level models are adopted to develop insights into the fracture processes and the prediction of the changes in mechanical properties. The benefits of these models to the arguments developed within safety cases which underwrite safe continued operation of these power stations are considered.

© 2003 Elsevier B.V. All rights reserved.

Keywords: Structural integrity; Material properties; Statistics; Mechanisms; Irradiation; Fracture

1. Introduction

Modelling materials and their engineering behaviour is used for a wide range of considerations in the nuclear electrical power generation industry. One purpose is directed towards demonstrating the design of new plant or safe continued operation of that plant in service. For this models have been developed over a wide range of scale dimensions. To describe mechanical and physical behaviour of materials a model is an idealisation that can be used simply to characterise a body of data at one extreme. At the other extreme, it is possible draw together the key physics of the problem so that the underlying mechanism is described and, thereby, it is possible to predict behaviour under conditions for which experimental data is not available. Models in the former category are essentially empirical and certainly cannot be used predictively beyond the range of the data. By comparison, physical models based upon established laws and principles of physics provide the opportunity to predict beyond the existing data. Several of these aspects of the use of models are appropriate for assisting with the solution of challenges

faced by the nuclear industry. We will address this by considering structural integrity requirements for the safe continued operation of nuclear electrical power generating plant. For this requirement, modelling is used to describe the material mechanical properties and potential failure mechanisms over a wide range of scale dimensions. Hence, models are used to describe experimental data sets, predict the response of materials under service conditions and understand basic mechanisms leading to changes in physical and mechanical properties.

We seek in this paper to explain by use of specific examples how various aspects of modelling are used to assist in demonstrating the safe continued operation of steel reactor pressure vessels at Magnox power stations. In [Section 2](#) we describe briefly operation and safety case requirements for reactor steel pressure vessels and in [Section 3](#) provide examples of modelling used to address different material aspects to support their operation and in [Section 4](#) we draw some overall concluding comments.

2. Magnox steel reactor pressure vessels

Magnox power stations with reactor steel pressure vessels operated by BNFL Magnox Generation were designed in the

* Corresponding author. Tel.: +44-1453-812-181;
fax: +44-1453-812-578.

E-mail address: peter.flewitt@magnox.co.uk (P.E.J. Flewitt).

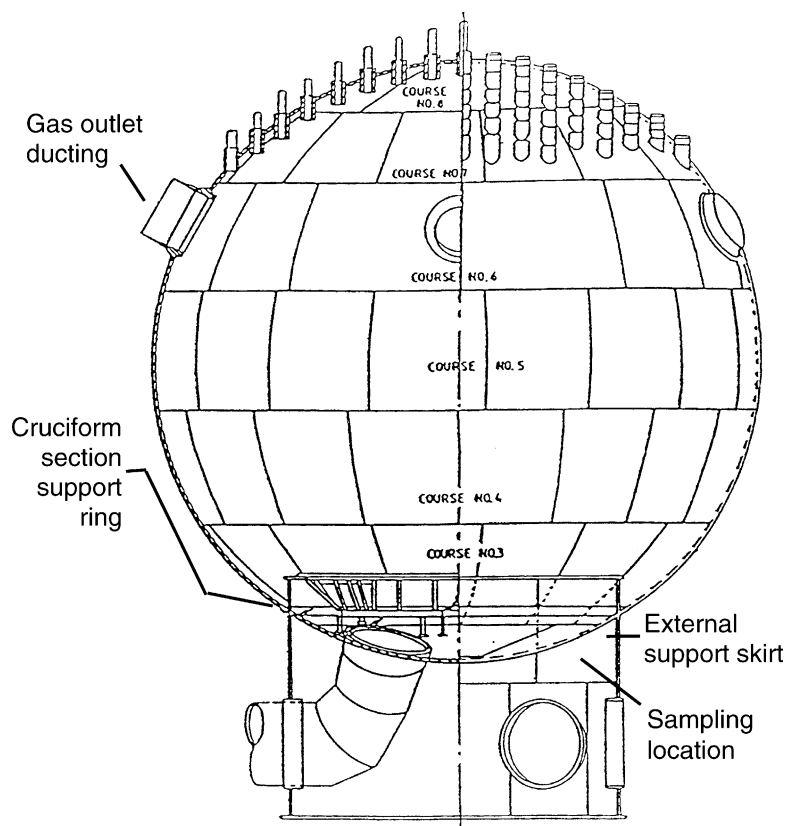


Fig. 1. Schematic diagram of a Magnox reactor steel pressure vessel. X is the general location of samples removed from the Trawsfynydd vessel.

1950s and 1960s against a requirement that failure in service should be incredible. Therefore, the vessels were designed and manufactured to the highest standards of the period and procedures were put in place to ensure that they were not operated outside their design limits. Since commissioning all the vessels have operated satisfactorily and changes to the properties of the steels used in their fabrication, as a result of exposure to neutron irradiation and service temperatures, have been monitored via in-reactor surveillance schemes. The safety cases to meet the requirement for continued operation beyond their original 25 year design life are based upon a multi-legged structural integrity safety argument.

Details of the later generation Magnox reactor steel pressure vessels are described elsewhere [1] but essentially they are 20 m diameter spheres fabricated from 75 to 100 mm thick carbon manganese steel plates and forgings joined together by either manual or machine made welds (Fig. 1). The spherical shell contains the carbon dioxide coolant gas and operates, typically, at a pressure of 1.8 MPa and a temperature of 360 °C. As with any structure of this type it is the welds that are judged to be the areas of the vessel most likely to contain any potential defects. The deterministic method of assessment has been described in detail elsewhere [1]. Briefly, a fracture mechanics approach is adopted based on the *R6* two criteria procedure [2]. The main inputs to the fracture mechanics assessment are: (i) depth, shape and position of a potential defect, (ii) materials properties, (iii) loading

conditions, and (iv) geometry of the component. This procedure is used to determine the minimum failure pressure as a function of vessel temperature, defined as the pressure limit line, for different locations on the vessel. By comparing this failure line with the pressure/temperature limits set by the operating rules it is possible to derive temperature margins and pressure reserve factors. Since the temperature and neutron flux are not uniform over the pressure vessel these assessments are undertaken at bounding and key locations.

3. Modelling pressure vessel materials

3.1. Introduction

The models adopted to provide material properties and understand the mechanisms and fracture modes are now considered. These span the scale range from the atom to large engineering structures.

3.2. Prediction of material properties

Materials mechanical property input data are required for the deterministic fracture mechanics reference defect assessment leg of the argument for the steel reactor pressure vessels as outlined in Section 2. This includes the start-of-life material properties for the submerged-arc weld metal

Table 1

Typical chemical composition (wt.%) for the reactor pressure vessel steel plate and forging, manual metal arc weld metal and submerged arc weld metal

	Element											
	C	Cr	Ni	Mo	S	Mn	P	Si	Cu	Sn	As	Al
Plate	0.15	0.03	0.06	0.01	0.035	1.15	0.02	0.17	0.10	0.012	0.018	0.057
Nozzle forging	0.18	0.07	0.08	0.01	0.024	1.30	0.024	0.36	0.10	0.015	0.029	0.049
Submerged arc	0.07	–	–	0.025	0.051	1.80	0.035	0.72	0.25	0.02	0.04	–
Manual metal arc	0.08	0.06	0.06	0.02	0.027	0.90	0.025	0.45	0.06	<0.01	0.032	<0.01

including yield stress, ultimate tensile stress and fracture toughness, together with the effect of neutron irradiation on these properties. As a consequence, a knowledge of the materials properties, particularly after exposure to the service environment, is an essential contribution to the overall structural integrity assessment. During service neutron irradiation at a given temperature degrades mechanical properties of the steel vessels, but in particular the submerged arc (SA) weldments [3] because of their higher copper content (Table 1) arising from the coating on the welding consumable. Prior to entering service the tensile properties were measured at ambient temperature and Charpy impact energy values obtained at a temperature of -10°C but no fracture toughness measurements were made. To supplement these data tensile and fracture toughness tests have been under-

taken over a wide range of temperatures on SA weld metal specimens obtained from archive material removed from the vessels at the time of construction to accommodate the inlet and outlet ducts. We will now explain how these data have been analysed and used within a range of modelling steps to derive fracture toughness values appropriate to the neutron dose and temperature at the various assessment locations on the reactor pressure vessel. The five key stages of the modelling are summarised in Fig. 2.

3.2.1. Stage 1: analysis of unirradiated fracture toughness data

Since the experimental data are limited by the amount of material available for fracture toughness testing a statistical analysis procedure was invoked that uses all the test data,

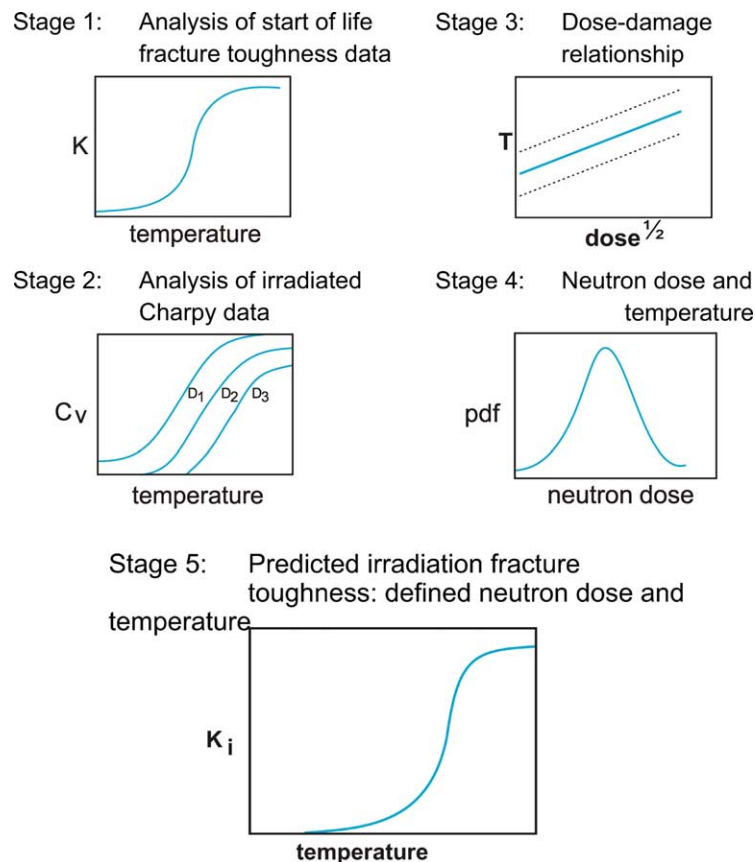


Fig. 2. The various stages of modelling, Stages 1–4, and analyses to predict the irradiated fracture toughness with temperature of C–Mn pressure vessel steel, Stage 6.

including that censored by unloading and terminating the fracture toughness test. For the latter the survival analysis approach was adopted [4]. The main analysis takes account of the competition between cleavage and ductile fracture modes in the ductile to brittle transition region using the recognised competing risk procedure. This provides the variation of the mean fracture toughness calculated from the SA weld metal database and the corresponding variation in the percentage of cleavage fracture with temperature (Fig. 2). The temperature at which there is 5% probability of cleavage fracture at initiation and 95% probability of 0.2 mm of prior ductile crack growth. This provides an appropriate statistical definition of the onset of the upper shelf temperature; an important temperature since it is accepted that at normal operating conditions the pressure vessels will be at or above the onset of the ductile to brittle transition.

3.2.2. Stage 2: analysis of irradiated Charpy impact energy data

Unfortunately, within the surveillance schemes for these steel reactor pressure vessels a relatively small number of specimens is available for a particular combination of SA weld metal, neutron dose and exposure temperature. By testing each set of specimens over a range of temperatures it is possible to construct a Charpy impact energy curve that is specific to a particular combination of service conditions and weld joint of a vessel. The irradiation surveillance data base is established by withdrawing, after certain periods of operation, batches of Charpy specimens subject to known service conditions. To define the temperature dependence of Charpy impact energy, each specimen is tested at a different temperature. Multiple tests at each temperature are rare due to the small number of specimens in a single batch. Moreover these data will be subject to three sources of scatter: (i) material or weld-to-weld variability, (ii) microstructural variability and (iii) that arising from the experimental procedure. Thus, scatter that would be observed in the experimentally measured values of Charpy impact energy if they were to be tested at the same test temperature would give rise to sampling errors in the estimated mean value of impact energy. The approach, based upon multiple regression, is used to accommodate the effect of neutron dose, dose rate and temperature on the overall Charpy impact transition curve.

Windle and co-workers [5] used a Burr distribution function to describe these data. Here, the variation of Charpy impact energy, C_V , with test temperature T_i is given by:

$$C_V = C_L + (C_U - C_L) \left(\frac{1 + \exp(T_i - T_0)}{\xi} \right)^{-\nu} + \varepsilon_i \quad (1)$$

where C_L is the lower shelf energy, C_U the upper shelf energy, ξ the gradient of the curve, T_0 locates the curve on the temperature axis, ν the shape parameter, Fig. 5 and ε_i the random error. The limits are $0 < 1 + \exp[(T_i - T_0)/\xi]^{-\nu} < +1$. The application of this model to obtain the Charpy impact energy mean curve employed maximum likelihood analysis. However, to obtain estimates of the uncertainty the analysis

was carried out in a Bayesian framework and implemented using Markov Chain Monte Carlo Sampling [6].

To predict the Charpy impact energy curves for a specific neutron irradiated and temperature condition it is necessary to express some of the model parameters in Eq. (1) as a function of the variables of dose, dose rate and temperature. These relationships can be obtained by considering the physical changes that occur in these steels as a result of neutron irradiation. According to mechanistic models [7], the temperature shifts in the impact energy curves are due to a combination of two hardening processes, copper and carbide precipitation and the formation of point defects within the matrix. In addition, there is one non-hardening process associated with brittle intergranular fracture brought about by impurity element segregation to, and embrittlement of, grain boundaries. An optimisation process is used to find a set of values for the model parameters that maximise the likelihood of the data. The error distribution can be estimated by calculating the residuals which are the difference between the measured Charpy impact energy values and the mean values predicted by the model using the estimated parameter. By using an optimisation routine it is possible to find a particular set of parameters that are the maximum likelihood estimate for the measured Charpy impact energy values.

3.2.3. Stage 3: dose–damage relationship

Although from Stage 2 the model provides the mean of the Charpy data and the interpretation of the confidence limits that quantify uncertainties in the Charpy impact energy values, on the ordinate, they cannot be translated into uncertainties in T_{40J} temperature on the abscissa. In the case of the SA weld metal used for the steel reactor pressure vessels it is the uncertainty in the T_{40J} temperature that is required to obtain a relationship between this parameter and neutron dose. Bayes theorem describes the relationship for a posterior probability $P(\theta/c)$ distribution, which is proportional to the product of a prior ($P(\theta)$) probability distribution and the likelihood ($L(\theta/c)$) of the Charpy impact energy data measured for a given set of model parameters such that:

$$P\left(\frac{\theta}{c}\right) = \left[\frac{P(\theta)L(\theta/c)}{\int P(\theta)L(\theta/c) d\theta} \right]. \quad (2)$$

In this expression $P(\theta)$ describes what is known about the model parameters without knowledge of the data. The likelihood $L(\theta/c)$ represents information about the model parameters coming from the data, in this case, defined as the likelihood of the particular model θ parameters given the measured Charpy impact energy data C . Since the measured Charpy impact energy data are fixed and there are many possible values of each model parameter and hence many different combinations, the likelihood function can be regarded as a function of θ . The integral in the denominator normalises the posterior probability distribution to unity. Each combination of model parameters can be used to calculate a single mean value of T_{40J} by inverting Eq. (1).

A plot of either temperature, T_{40J} , or the temperature shift, ΔT_{40J} , against the likelihood for each possible combination of model parameters defines the probability distributions for these quantities. To obtain uncertainties in T_{40J} or ΔT_{40J} it is necessary to establish the likelihood surface appropriate to a particular set of data and a statistical model. Methods for computation of posterior distributions have been discussed by, Smith and Roberts [8] and Smith and Markov [9] the latter involving Markov Chain Monte Carlo sampling of the likelihood surface. Hence, the Bayesian estimates describe the probability distribution of all possible T_{40J} values. The distribution of these temperatures T_{40J} plotted against neutron irradiation dose, $D^{1/2}$, gives a dose–damage relationship with a mean and the associated probability intervals to describe the uncertainty (Fig. 2). Thus, we have the necessary information to evaluate the fracture toughness of material in the neutron-irradiated condition if this is combined with a experimentally established correlation between Charpy impact energy and fracture toughness [10].

3.2.4. Stage 4: neutron dose and temperature

To quantify the neutron doses for the pressure vessels, detailed neutron dosimetry models have been developed for each reactor based on a Monte Carlo radiation transport code (MCBEND) [10]. This code allows an explicit geometrical representation of the reactor cores, support structures and vessels and has a neutron energy resolution to enable changes in neutron spectra to be modelled. To predict the change to materials properties at different positions in a pressure vessel estimates of the total dpa dose are made. The effects of changes to component dimensions and operational practices on dose distributions are represented to provide fast and thermal neutron lifetime averaged doses at all vessel locations. The pressure vessels are equipped with thermocouples to provide on-line indications of operational temperatures. Appropriate boundary conditions are used in computational fluid dynamics models to enable vessel temperatures to be assessed at locations between measurement points.

3.2.5. Stage 5: predicted fracture toughness and validation

The inputs described in Stages 1–4 are drawn together via a program, CUSURV to predict the irradiated fracture toughness of a given assessment location on the pressure vessel [10]. Following decommissioning of the Magnox reactor at Trawsfynydd, a sampling programme was undertaken for a region of a pressure vessel exposed to neutron irradiation at low temperature and high neutron dose [10]. An objective was to compare measured service fracture toughness data with that predicted by the modelling methodology. The pressure vessel location selected for sampling maximised the lengths of the available SA weld metal and provided a relatively uniform neutron dose profile with a known and constant service temperature. This region was located below-core where the irradiation

temperature was about 187 °C and the mean inner surface dose was about 350×10^{-5} dpa. Access to these welds was from the outside of the pressure vessel, but within the support skirt (Fig. 1), so that a number of specialised remotely-operated vehicles were constructed to bear cutting and manipulating tools. The cutting method selected was a high power jet of abrasive particles suspended in water [10]. Four different SA welds were sampled providing from each weld four tapered, through-wall, plugs of 150 mm diameter. From a plug Charpy geometry fracture toughness specimens were machined at four differently dosed layers through the wall thickness. The test method selected was quasi-static three-point bend fracture toughness testing, permitting direct comparison with the predictive method used for calculating the toughness of the irradiated material. The results obtained from the overall fracture toughness test programme are compared with the predictions from the overall materials modelling (Fig. 3). These measured fracture toughness data support the methodology adopted for predicting service exposed material property changes.

3.3. Mechanistic modelling

We will now consider three examples of modelling that provide an improved understanding of the role of various mechanisms that contribute to the changes in material properties or fracture processes considered in Section 3.2.

3.3.1. Neutron irradiation damage

Defect production in metals subjected to fast neutron irradiation from power reactor cores is initiated by displacement cascades. Molecular dynamics (MD) computer simulation provides a powerful means of investigating these events and the atomic mechanisms that lead to defect production and clustering in cascades have been reviewed elsewhere [11]. In general, these atomic scale models have considered single cascades whereas over the lifetime of reactor steel pressure vessels (Fig. 1), they can be produced in debris of earlier cascades. The effects on defect production of the overlap of collision cascades in α -iron provides an insight in to this underlying contribution [12]. The model size employed is either a cube of side $30a$ or $40a$ where a is the bcc lattice parameter. The MD program used was the vectorised MOLDY code modified for the bcc structure [11]. To simulate a cascade, a block was first equilibrated for ≥ 10 ps at a temperature of 100 K. After the primary knock-on atom was initiated the crystal was allowed to evolve for ~ 10 ps. The crystal containing the defects created by this cascade was quenched to 0 K, re-equilibrated at 100 K and the overlap cascade event initiated. The approximations in the model are: (i) heat is not extracted from the cell after the cascade had started, (ii) there is no electron phonon coupling and (iii) the cohesive term in the many-body inter-atomic potentials is isotropic and does not include the angular nature of bonding. These approximations are reasonable within the

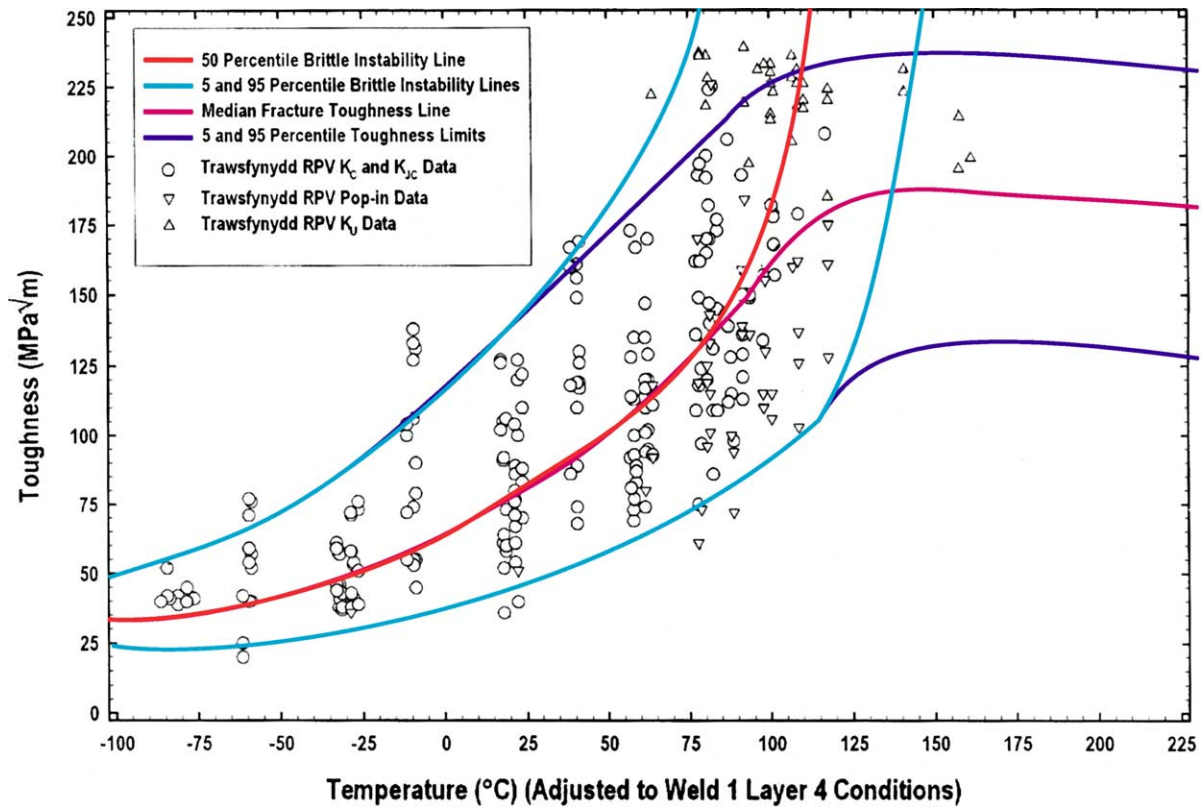


Fig. 3. Fracture toughness data, K_{IC} or K_{IC} as a function of temperature compared with CUSURV prediction

context of overall capability in large-scale MD modelling of damage. Here, the appropriate separation parameter is the distance, R_{pp} , between the centre of gravity, C_2 , of the displaced atoms of this cascade at the time of the peak in damage and the equivalent point, C_1 , in the initial cascade (Fig. 4).

The data for the final number of Frenkel pairs as a function of separation, R_{pp} , for four sets of overlap conditions at 100 K is given in Fig. 5. There is a clear trend towards decreasing defect numbers as the overlap distance decreases. Two cascade energies considered are very different, 400 eV and 5 keV, corresponding to thermal and fast neutron

Cascade overlap: (cascade 2 overlaps cascade 1)

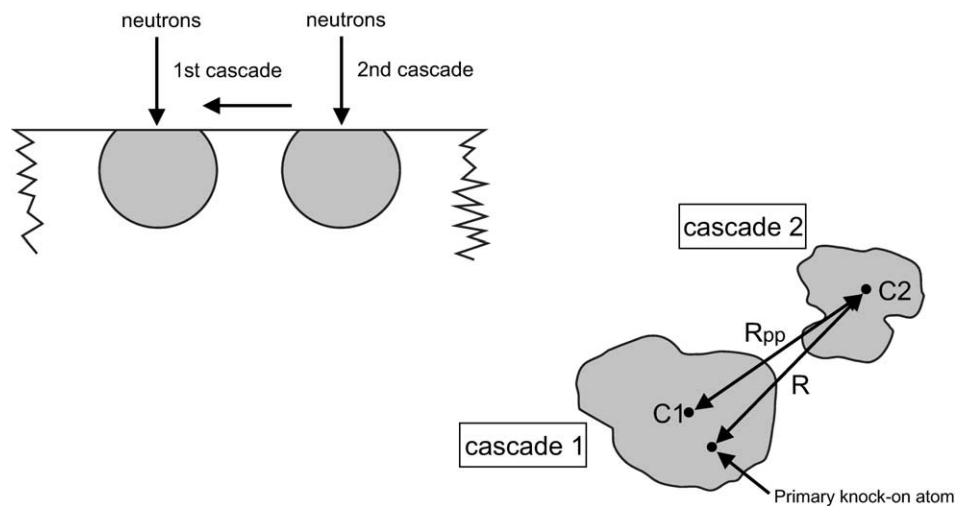


Fig. 4. The centre of gravity of the displaced atoms at the peak of the damage of the initial cascade 1 at point C_1 . The second overlap cascade 2 caused by a PKA a distance R from C_1 has its damage centred on C_2 , a distance R_{pp} from C_1 .

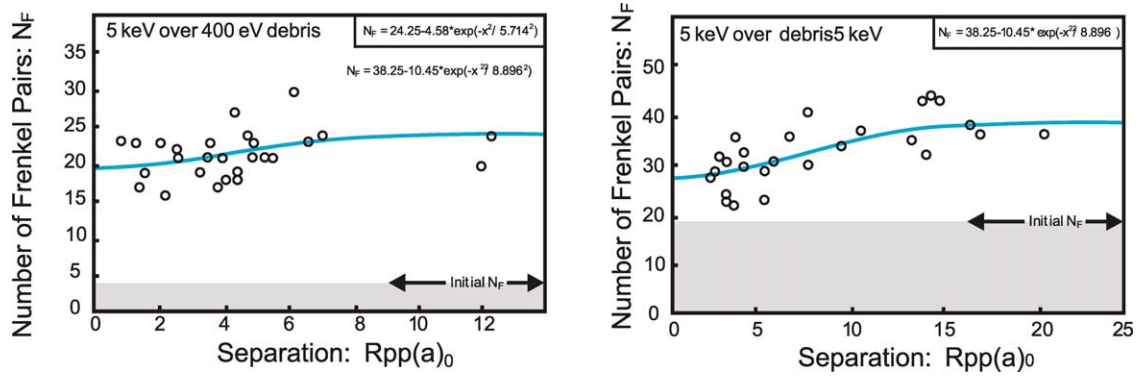


Fig. 5. The total number of Frenkel pairs remaining after the cascade overlap simulations in a crystal at 100 K is plotted as a function of separation parameter R_{pp} for the four different energy conditions considered, as indicated. The value of N_f for the initial cascade is given and the best fit of Eq. (3) to the data is shown in the inset.

energies. In this case, defects produced by the smaller energy cascade are effectively lost at complete overlap, regardless of the cascade sequence. The same effect was found even for two cascades of the same energy of 2 keV. When both cascades have the higher energy of 5 keV the scale loss is reduced to about half of the value for a single cascade. Clearly, the mechanisms that result in defect loss in overlap events, compared with non-overlapping cascades, depend upon the chosen kinetic energy. For the 400 eV cascades, pre-existing damage in the lattice shortens the replacement sequences and hence assists and recombination of vacancies and interstitials or it recombines with a smaller number of defects created in the second cascade. When the kinetic energy is large most of the loss occurs when the hot, disordered core of the second cascade envelops the defects produced by the first. This example demonstrates how modelling at the atomic scale provides an insight into the development of point defect damage that leads to changes in yield strength and fracture toughness of pressure vessel steels.

3.3.2. Irradiation-induced segregation

Irradiation-induced segregation to grain boundaries can be described by inverse Kirkendall models or solute-point-defect complex models [13]. Such segregation can have a significant effect on the non-hardening contributions to the shift in the ductile to brittle transient-curve for pressure vessel steels described in Section 3.2. Certainly this can lead to a change in the brittle fracture mode from cleavage to intergranular. The approach has been extended to evaluate the maximum concentration of non-equilibrium segregation in ternary alloys through the following considerations. As stated by Faulkner et al. [14], the absolute concentration of complexes is proportional to the solute concentration and the exponential term containing the solute-point-defect binding energy. To evaluate the effect of site competition between two solutes on the maximum concentration of irradiation-induced non-equilibrium segregation, the $C_{br(Sj)}^m$ modified absolute concentrations of

complexes in the ternary situation may be included. So that the maximum concentration is given by:

$$C_{br(Sj)}^m = C_g^{Sj} \frac{E_{b(Sj)}^{ip}}{E_f^p} \left[\frac{C_g^{Sj} \exp(E_{b(Sj)}^{ip}/kT)}{\sum_j C_g^{Sj} \exp(E_{b(Sj)}^{ip}/kT)} \right] \times \left[1 + \frac{BGF(\eta)}{A_p D_p k_{jp}^2} \exp\left(\frac{E_f^p}{kT}\right) \right], \quad j = 1, 2 \quad (3)$$

$E_{b(Sj)}^{ip}$ is the soluble j -point-defect binding energy, and C_g^{Sj} the matrix concentration of solute j , p stands for the point-defect, either the vacancy, V , or the interstitial I , D_p the diffusion coefficient of point-defects in the matrix, E_b^{ip} the solute-point-defect binding energy, E_f^p the point-defect formation energy, A_p a constant associated with the vibrational entropy of atoms around the point-defect, G the point-defect production rate (or neutron dose rate), k the Boltzmann constant, T the absolute temperature, η a long range recombination term, B the dose rate correction factor, i.e. the fraction of freely migrating point-defects escaping from the cascade k_{jp}^2 , and k_{dp}^2 is the sink strength for point-defects. The kinetics for irradiation-induced grain boundary segregation are given by:

$$\frac{C_{br(Sj)}^{Sj}(t) - C_g^{Sj}}{C_{br(Sj)}^m - C_g^{Sj}} = 1 - \exp\left[\frac{4D_{c(Sj)}^{ip}}{\alpha_{n(Sj)}^2 d^2}\right] \times \operatorname{erfc}\left[\frac{2(D_{c(Sj)}^{ip})^{1/2}}{\alpha_{n(Sj)} d}\right] \quad j = 1, 2 \quad (4)$$

where $C_{br(Sj)}^{Sj}(t)$ is the concentration of solute j at the concentrated layer as a function of irradiation time at a given irradiation temperature. $D_{c(Sj)}^{ip}$ is the diffusion coefficient of solute j -point-defect complexes, and $\alpha_{n(Sj)} = C_{br(Sj)}^m / C_g^{Sj}$.

The model has been applied to the segregation of phosphorous in a Fe–C–P alloy subjected to neutron irradiation.

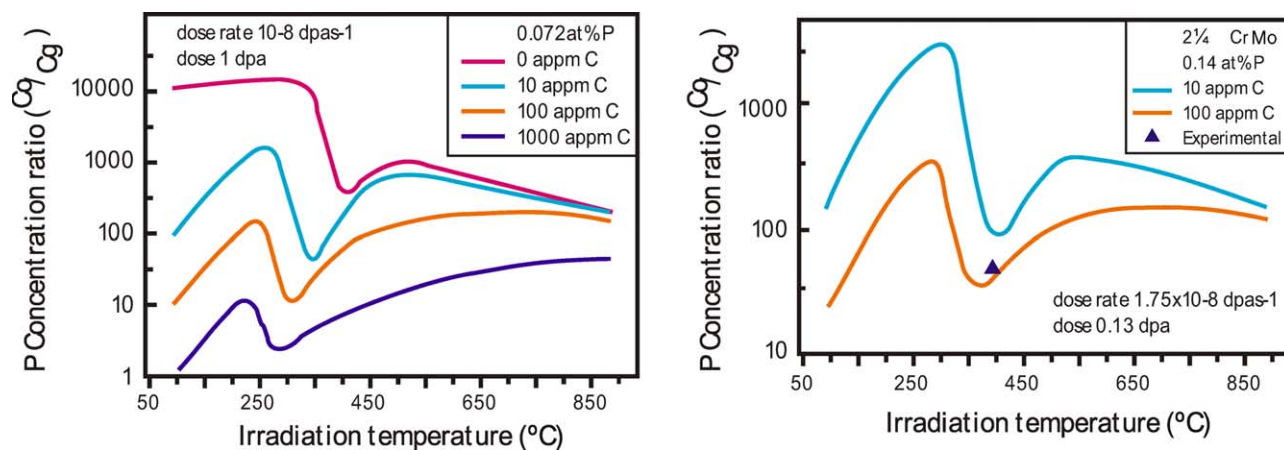


Fig. 6. The grain boundary segregation of P during neutron irradiation for: (a) Fe: 0.072 at.% P–C (0, 10, 100 and 1000 appm C) alloy, ($p_0 = 10^{16} \text{ m}^{-2}$, $R = 10 \mu\text{m}$, dose rate $= 10^{-8} \text{ dpa s}^{-1}$ dose to 1 dpa). (b) Neutron irradiation in Fe–C–0.14 at.% P alloys as a function of irradiation temperature, predicted for different free carbon concentrations and with irradiation conditions: dose rate $= 1.75 \times 10^{-8} \text{ dpa s}^{-1}$ and dose $= 0.13 \text{ dpa}$. The experimental mean value is plotted for comparison (grain size $= 10 \mu\text{m}$ and dislocation density constant $= 10^{15} \text{ m}^{-2}$, and pre-irradiation boundary concentration $= 3.8 \text{ at.}\%$).

Here, solute–interstitial and solute–vacancy complex contributions are treated separately to determine if one is dominant in neutron irradiation-induced non-equilibrium segregation. Data used for these calculations are given elsewhere [14]. The predicted grain boundary segregation of phosphorous during neutron irradiation, for this the site competition model with different free carbon concentrations, is given in Fig. 6(a) as a function of irradiation temperature. Clearly phosphorous segregation is shown to be suppressed, notably at lower temperatures, due to the competition of carbon with phosphorous for segregation sites. Carbon segregation is dominant in this alloy and is somewhat influenced by the site competition of phosphorous with carbon in the high-temperature range. This indicates that grain boundary segregation of phosphorous during neutron irradiation in pressure vessel steels is predicted to be restrained, especially at lower temperatures, by minor changes in free carbon content in the ferritic phase. However, dissolved carbon content, in reality, is extremely low in commercial structural steels. A comparison of predictions from this ternary site competition model with some experimental values obtained by Song [15] for the phosphorous segregation is shown in Fig. 6(b). The predictions are made for different free carbon contents

and with the following irradiation conditions: neutron dose rate $= 1.75 \times 10^{-8} \text{ dpa s}^{-1}$ and neutron dose $= 0.13 \text{ dpa}$. The experimental data are for a 0.14 at.% phosphorus-doped 2.25Cr1Mo steel at temperatures of 400 $^{\circ}\text{C}$. There is a reasonable fit between the predictions and the observations if a realistic free carbon content is used. The model points to the important role of free carbon in the ferritic phase influencing the amount of phosphorous segregation to grain boundaries in pressure vessel steels when subject to neutron irradiation. This will modify the proportion of intergranular fracture and potentially the lower shelf and transition fracture toughness.

3.3.3. Fracture processes

We will now consider modelling to describe fracture processes that can occur in ferritic steels at the micro-scale. In Section 3.2, we considered modelling Charpy impact energy data relevant to steel reactor pressure vessels with respect to the influence of neutron irradiation. This has then been used to predict the effect of irradiation on the fracture toughness and the ductile to brittle transition temperature. In these cases, the lower shelf fracture is considered to occur predominantly by transgranular cleavage. However,

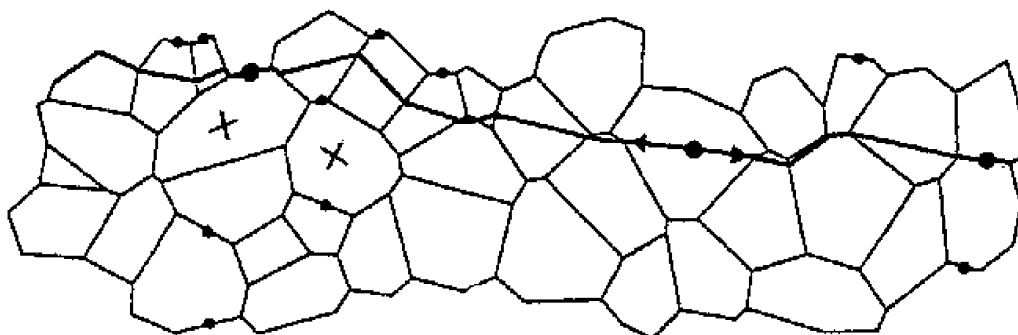


Fig. 7. The 2D model used in the calculation of the effect of grain boundary embrittlement arising for a change in composition.

in addition to cleavage fracture, brittle inter-granular fracture can arise if certain alloying or impurity elements, to grain boundaries [13]. Of particular interest, as shown in Section 3.3.2, is the segregation of phosphorus to grain boundaries.

Various three-dimensional (3D) and two-dimensional (2D) models have been developed [16,17]. For the 3D models the well known array of tetrakaidcahedra (14-hedra) filling space has been adopted together with various extensions to these. In the simple applications, it is assumed that crystallographic orientations of grains are distributed randomly, only cleavage or brittle grain boundary failure may occur, cleavage is on one of three variants of $\{100\}$ and fracture facets are as close as possible to being perpendicular to the stress axis; to model more complex situations these assumptions are relaxed. To model the embrittlement of grain boundaries arising from segregation of impurity elements the relative energies of boundaries have to be considered. In particular, a ratio cleavage to grain boundary

fracture energy, a range of grain boundary energies, a possible bias of grain boundary energies and a possible bias of grain boundary energies according to orientation relative to the stress axis have to be introduced. Because of the complexity of constructing, using and visualising 3D models, where possible, 2D models have been adopted. Here, models based on random arrays of polygons have been adopted, an example of part of such an array is shown in Fig. 7. The models are generated by locating grain nuclei randomly and drawing Wigner-Seitz cells around them. Each grain is given a random crystallographic orientation which defines potential cleavage planes and, where appropriate, slip planes. In some applications, the models are stretched so that the grains become elongated and the orientations are biased to represent textures of rolled materials.

To use the models to investigate the nature of fracture surfaces, energies E_c and E_g are allocated for cleavage and grain boundary fracture, respectively, [18]. A crack is then nucleated on a cleavage plane or a grain boundary, selected

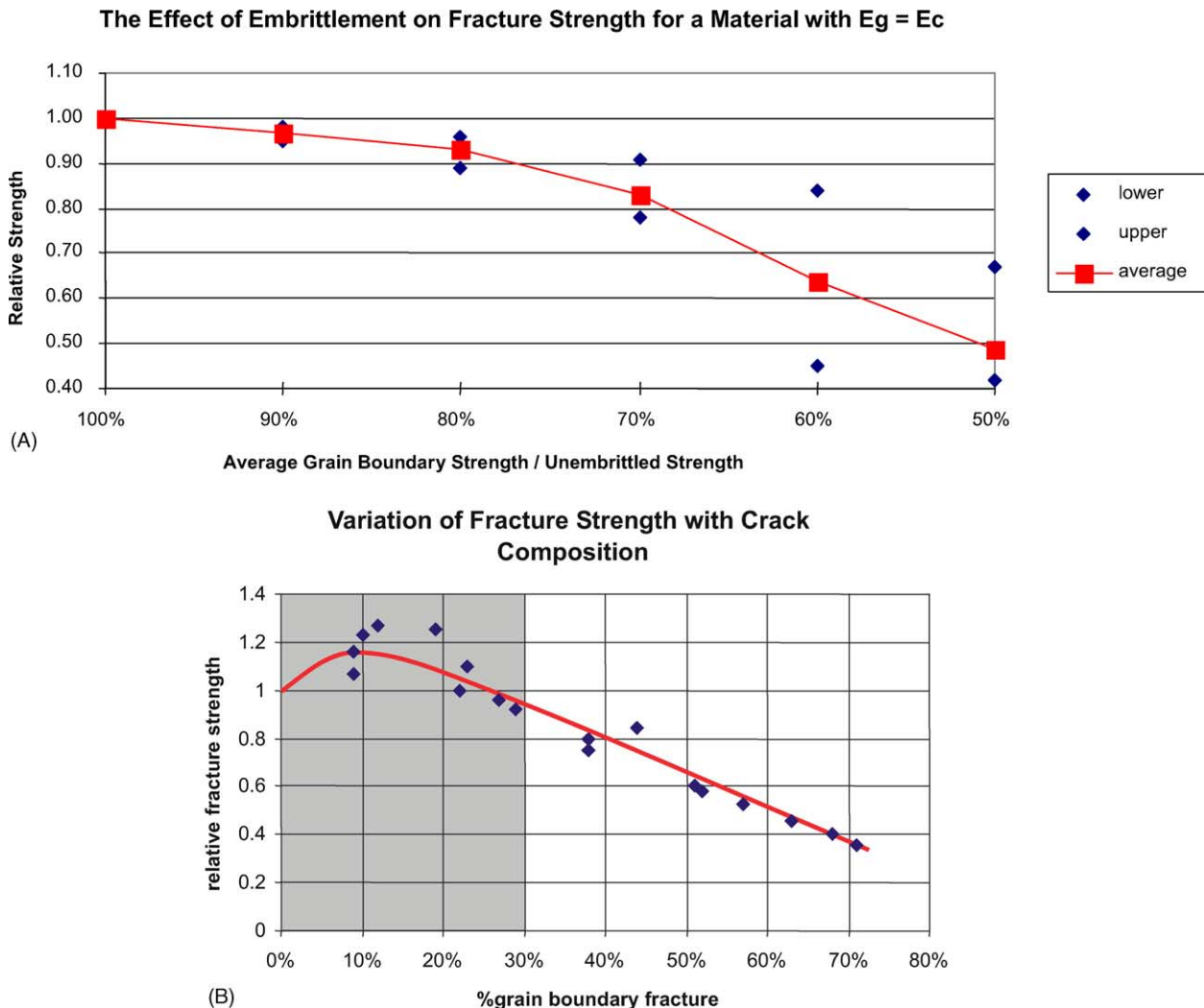


Fig. 8. The effects of embrittlement of grain boundaries in: (A) fracture strength bcc iron (with $E_g = E_c$) with average grain boundary strength to unembrittled strength and (B) relative fracture strength with percentage of intergranular fracture.

because it has a favourable orientation relative to the stress axis and a large dimension. When the crack reaches a grain boundary or occasionally a grain corner the adjacent grain boundary orientations and the appropriate energies are examined to determine how the crack will propagate. This is repeated until the crack has crossed the whole model. It is possible to consider how a brittle crack propagates across the model with grain boundaries and crystallographic orientations randomly generated, with two on the general cleavage planes in each grain and with E_g and E_c having a range of values. This process was repeated for a range of ratios of E_c/E_g between 4 and 0.25 the former corresponding to different amounts of segregation. As time increases to model embrittlement the weak grain boundaries are assumed to become weaker, as more segregation occurs, causing a progressive weakening of selected boundaries. In the model, this is simulated by reducing grain boundary strengths by an amount inversely proportional to the difference squared between their initial strength and the maximum strength so that:

$$E_i(k) = a[E_{\max} - E_i(0)]^2 \quad \text{for edge } i - 7 \quad (5)$$

where a is chosen to give the required reduction in E_g . This relationship reduces the strength of grain boundaries preferentially and reflects the dimensional change for a uniform distribution of impurity atoms segregated along, the 1D grain boundary. The selected embrittlement also reduces the average grain boundary energy, E_g . The model is fractured again with the same starting point for the crack and the crack path analysed. The result of embrittlement on the fracture strength for a relative strength of E_g/E_c of unity is shown in Fig. 8(A). When the grain boundaries are initially weak compared with the cleavage fracture energy embrittlement does not at first decrease the fracture strength significantly. It is only when embrittlement reaches about 20–30% that the strength falls rapidly. The main difference when the ratio E_g/E_c increases to 4 is that the fracture strength decreases approximately linearly as embrittlement increases. Fig. 8(B) shows the variation of fracture energy with percentage of intergranular fracture. Here there is a non-linear decrease with little variation in the fracture energy with up to about 20% intergranular fracture. This latter information provides a guide to the significance of the proportion of coverage of grain boundaries by, for example, impurity phosphorus on the brittle fracture strength and, indeed, the fracture toughness of pressure vessel steels. Clearly segregation can lead to a significant proportion of intergranular fracture without causing to a deterioration of the fracture toughness of the material. Such a conclusion has important implications for understanding the response of the pressure vessel steels to neutron irradiation induced grain boundary segregation.

4. Concluding comments

In general multiscale modelling provides a powerful tool to assist in interpreting and predicting materials property data that one required as an input to the assessment of Magnox steel reactor pressure vessels. As a consequence such modelling is an essential contribution for underwriting the safe, continued operation of steel reactor pressure vessels.

Acknowledgements

The author would like to thank Professors D.J. Bacon, A.G. Crocker and R.G. Faulkner and Dr. R. Moskowic for their helpful collaboration. This paper is published with the permission of the Head of Reactor Services, BNFL Magnox Generation.

References

- [1] P.E.J. Flewitt, in: A. Bakker (Ed.), *Structural Integrity Assessment of High Integrity Structures and Components: User Experience, Mechanical Behaviour of Materials*, Delft University Press, Delft, 1995.
- [2] I. Milne, R.A. Ainsworth, A.R. Dowling, A.T. Stewart, *Assessment of the Integrity of Structures Containing Defects*, CEBG Report R/H/R6 Rev 3, 1986.
- [3] C.A. English, A.H. Fudge, R.J. McElroy, W.J. Phythian, J.T. Buswell, R.B. Jones, *Int. J. Pressure Vessels Piping* 54 (1993) 49.
- [4] R. Moskowic, *Eng. Frac. Mech.* 44 (1993) 21.
- [5] R. Moskowic, P.L. Windle, A.E. Smith, *Met. Mater. Trans.* 28A (1997) 1181.
- [6] R. Moskowic, P.E.J. Flewitt, *Met. Mater. Trans.* 28A (1997) 2609.
- [7] C.J. Bolton, J.T. Buswell, R.B. Jones, R. Moskowic, R.H. Priest, in: *Proceedings of the 11th International Symposium of ASTM*, STP1270, ASTM Phila, PA, 1996, p. 103.
- [8] A.F.M. Smith, G.O. Roberts, *J. R. Stat. Soc. B55* (1993) 3.
- [9] A.F.M. Smith, A. Markov, *Chain Monte Carlo Model for Statistical Analysis of Charpy Data*, Nuclear Electric Report TEX/REP/0001/95, Nuclear Electric, London, 1995.
- [10] P.E.J. Flewitt, C.J. Bolton, D.J. Edens, *Assuring It's Safe*, Ist Mech. Eng. Conf. Trans., Prog. Eng. Publishers, London, 1998, p. 103.
- [11] D.J. Bacon, T. Diaz de la Rubia, *J. Nucl. Mater.* 216 (1994) 275.
- [12] F. Gao, D.J. Bacon, A.F. Calder, P.E.J. Flewitt, T.A. Lewis, *J. Nucl. Mater.* 230 (1996) 47.
- [13] P.E.J. Flewitt, R.K. Wild, *Grain Boundaries: Structure and Composition*, Wiley, Chichester, 2000.
- [14] R.G. Faulkner, S.H. Song, P.E.J. Flewitt, M. Victoria, P. Marmy, *J. Nucl. Mater.* 255 (1998) 189.
- [15] S.H. Song, Ph.D. Thesis, Loughborough University, Leic., UK, 1995.
- [16] A.G. Crocker, G.E. Smith, P.E.J. Flewitt, R. Moskowic, *Mater. Sci. Forum* 294–296 (1999) 673.
- [17] G.E. Smith, A.G. Crocker, R. Moskowic, P.E.J. Flewitt, *Phil. Mag.*, in press.
- [18] G.E. Smith, A.G. Crocker, P.E.J. Flewitt, R. Moskowic, submitted for publication.